# pH-Activated Dynamic Ionomer-Acetal Networks for Self-Healing and Recyclable Electrophoretic Acrylic Coatings

Sushmit Sen, Sourav Ghosh, Amrita Chatterjee, Pradip K. Maji*

Department of Polymer and Process Engineering, Indian Institute of Technology Roorkee, Saharanpur Campus, Saharanpur- 247001, India

*Corresponding Author: Pradip K. Maji (Email ID: pradip@pe.iitr.ac.in);

Contact no: +91-7895965010

## Section 1-S: Materials, Methods and Characterisation Techniques

### Materials

Multi-walled carbon nanotubes (MWCNTs-OH, length 10-30 μm, diameter 10-20 nm), Hexadecyltrimethylsiloxane (HDTMS), ammonium hydroxide solution, and anhydrous ethanol were procured from Sigma Aldrich. The deionized water used in the experiments were handmade in the laboratory. The monomers methyl methacrylate (MMA), butyl acrylate (BA), and dimethylaminoethyl methacrylate (DMAEMA) were purchased from TCI Chemicals, India. The initiator 2,2′-azobis(2-methylpropionitrile) (AIBN) and the crosslinker Glutaraldehyde (GA) was purchased from HiMedia, India. No further purification of the reagents was carried out. M/S SBL Specialty Coatings, India very kindly supplied the aluminium (Al) substrates.

### Electrophoresis Process

During cathodic electrophoresis, the lactic-acid–protonated acrylic ionomer particles, carrying cationic ammonium groups, migrate toward the cathode under the applied electric field. At the cathode surface, water reduction generates hydroxide ions ($2H_2O + 2e^- \rightarrow H_2 + 2OH^-$), which raises the local pH. This increase in pH deprotonates the ammonium groups of the ionomer, reducing their water solubility and triggering coagulation at the electrode–solution interface. As a result, a uniform and adherent polymer film is deposited directly on the cathode surface, with deposition continuing until the growing film becomes sufficiently insulating. Prolonged cathodic electrophoresis (50 V for 40-60 s) resulted in a significant increase in coating thickness; however,

the films became highly porous and exhibited a spongy, non-continuous morphology. Similar behavior was observed at higher voltages (55-60 V for 30 s), where rapid deposition led to film defects and loss of uniformity. Therefore, deposition time and voltage were optimized to balance thickness and film integrity. Thus, although electrophoretic migration contributes to transport of charged ionomer particles, film deposition is ultimately governed by electrochemically induced pH shifts at the cathode, consistent with the mechanism of conventional cathodic electrophoresis (CED) coatings. (**Fig. S1**).

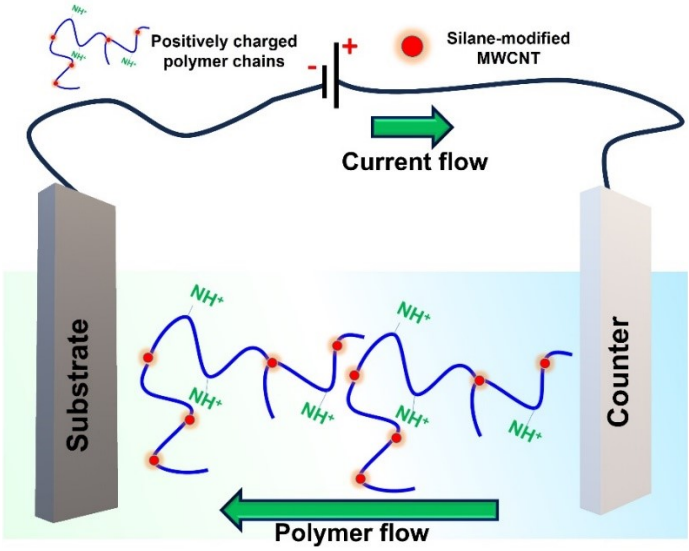


***Fig. S1****: Electrophoresis of the Coatings*

**Characterization Techniques**

The chemical structure of the acrylic resin was probed by Fourier-transform infrared spectroscopy (FTIR, PerkinElmer Spectrum Two, ATR mode, 400-4000 $cm^{-1}$, 4 $cm^{-1}$ resolution), while Raman spectroscopy (Renishaw Invia, 532 nm excitation, 800-2000 $cm^{-1}$) provided complementary vibrational fingerprints of the polymer-nanofiller network. Surface chemistry and bonding environments were analyzed by X-ray photoelectron spectroscopy (XPS, PHI-5000 Versa Probe III, Al Kα source, 280 eV survey and 55 eV high-resolution scans, C 1s at 284.6 eV as reference). Morphology and dispersion were examined by field-emission scanning electron microscopy (FESEM, TESCAN MIRA3, 5-10 kV) with energy-dispersive X-ray analysis (EDAX, AMTEK) and atomic force microscopy (AFM, Bruker Dimension Icon, Scan Assist mode), while water contact angles (WCA) were measured using the sessile drop method (DSA25 KRÜSS, 5 µL

droplets, room temperature). DSC analysis was carried out on a TA Discovery DSC25P using aluminum pans with pierced lids under nitrogen purge (50 mL $min^{-1}$). Approximately 5–8 mg of each sample was dried at 60 °C under vacuum for 12 h before sealing. Measurements were performed at a heating rate of 10 °C $min^{-1}$ from -50 °C to 600 °C, with the endothermic (endo) and exothermic (exo) directions indicated on the thermograms. Coating quality was assessed via dry film thickness (DFT, Elcometer 456, ASTM D7091-13), cross-cut adhesion (ASTM D3359), and pencil hardness (ASTM D3363). Electrochemical impedance spectroscopy (EIS, CHI162IE, 3.5% NaCl, 100 kHz–10 mHz, 10 mV amplitude) was employed to quantify barrier and corrosion resistance, with immersion testing performed according to ASTM G31.[1,2] Anti-icing and photothermal de-icing were examined under Xenon lamp, wavelength of 2500-750 nm, NIR and the energy of the incident wavelength corresponds to 0.50 eV to 1.77 eV, monitored with IR thermal imaging, IRay C2000+), as well as under ambient solar light, while ice layers were prepared at -40 °C. Finally, recyclability was assessed via solvent-assisted recovery of crosslinked films, wherein fragmented samples were swollen, reprocessed, and recast into continuous coatings exhibiting mechanical stability comparable to pristine films.

**Section 2-S: Determination of Copolymer Composition by $^1$H NMR**

The molar composition of the synthesized copolymer was determined using $^1$H NMR spectroscopy by integrating characteristic proton signals corresponding to each monomer unit. The methoxy protons of methyl methacrylate (MMA, $–OCH_3$) at ~3.6 ppm (3H), the methylene protons of butyl acrylate (BA, $–OCH_2–$) at ~4.1 ppm (2H), and the dimethylamino protons of DMAEMA ($–N(CH_3)_2$) at ~2.3 ppm (6H) were selected for analysis due to minimal peak overlap.

The molar contribution of each monomer was calculated by normalizing the integrated peak areas (I) with respect to the number of contributing protons (n), according to:

$$N_i = \frac{I_i}{n_i} \quad \text{(eqn. S1)}$$

where $N_i$ is the relative molar amount of monomer $i$, $I_i$ is the integrated peak area, and $n_i$ is the number of protons responsible for the selected signal.

The molar percentage of each monomer was then calculated using:

$$\text{mol\%}_i = \frac{N_i}{\sum N_i} \times 100 \quad \text{(eqn. S2)}$$

Using the experimentally obtained integrals:

- $I_{\text{MMA}} = 1.00$, $n = 3$
- $I_{\text{BA}} = 0.37$, $n = 2$
- $I_{\text{DMAEMA}} = 0.53$, $n = 6$

the normalized molar contributions were calculated as:

$$N_{\text{MMA}} = \frac{1.00}{3} = 0.33$$

$$N_{\text{BA}} = \frac{0.37}{2} = 0.185$$

$$N_{\text{DMAEMA}} = \frac{0.53}{6} = 0.088$$

Total:

$$\sum N_i = 0.33 + 0.185 + 0.088 = 0.598$$

Thus, the molar composition was obtained as:

$$\text{MMA} = \frac{0.33}{0.598} \times 100 \approx 55\%$$

$$\text{BA} = \frac{0.37}{0.598} \times 100 \approx 30\%$$

$$\text{DMAEMA} = \frac{0.088}{0.598} \times 100 \approx 14\%$$

Therefore, the copolymer composition was determined to be approximately **55:30:14 (MMA:BA:DMAEMA, mol%)**. The selected peaks ensured minimal overlap and reliable quantification, and the obtained composition shows good agreement with the initial monomer feed

ratio (**54:36:12**), with minor deviations attributed to differences in monomer reactivity during free-radical copolymerization.

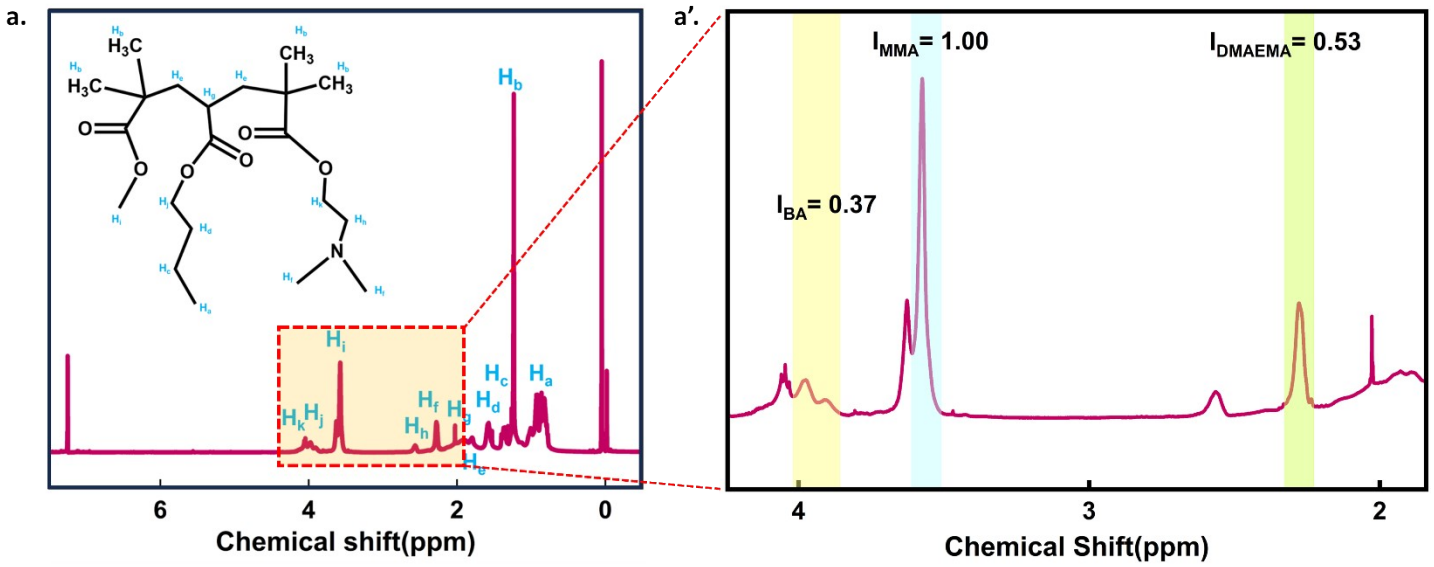


***Fig. S2****. a. NMR spectrum of the synthesized resin; a' enlarged area of the NMR spectrum show the non-overlapping areas of the specific monomers: methoxy protons of methyl methacrylate (MMA, –$OCH_3$) at ~3.6 ppm (3H), the methylene protons of butyl acrylate (BA, –$OCH_2$–) at ~4.1 ppm (2H), and the dimethylamino protons of DMAEMA (–$N(CH_3)_2$) at ~2.3 ppm (6H)*

**Section 3-S: Self-Healing under variable pH**

The influence of pH on the thermal self-healing behavior of the coatings was investigated by monitoring crack closure as a function of temperature and healing environment. A clear pH dependence was observed for the temperature required to achieve complete healing. At pH 2, full crack closure occurred at 80-85 °C, whereas pH 4 required a higher temperature of approximately 100 °C. In contrast, samples at pH 6 exhibited complete healing only at significantly elevated temperatures (120-125 °C).

To further isolate the role of pH from thermal effects, additional healing experiments were conducted at a fixed temperature of 65 °C for all three pH conditions (pH 2, 4, and 6). Under these conditions, complete healing was not achieved within 20 min for any sample; however, pronounced differences in crack evolution were evident (**Fig. S2**). The pH 2 sample showed

substantial crack narrowing and edge smoothing, pH 4 displayed partial recovery, while pH 6 exhibited minimal change in crack morphology.

Because the temperature was held constant, these differences cannot be attributed to thermal softening. Instead, the results indicate that acidic conditions enhance dynamic acetal/hemiacetal exchange, facilitating chain-segment transfer even under sub-optimal thermal conditions. Collectively, the pH-dependent healing temperatures and fixed-temperature comparison confirm that the self-healing response is primarily governed by chemically activated dynamic bond exchange coupled with ionomer-assisted chain mobility rather than temperature alone.

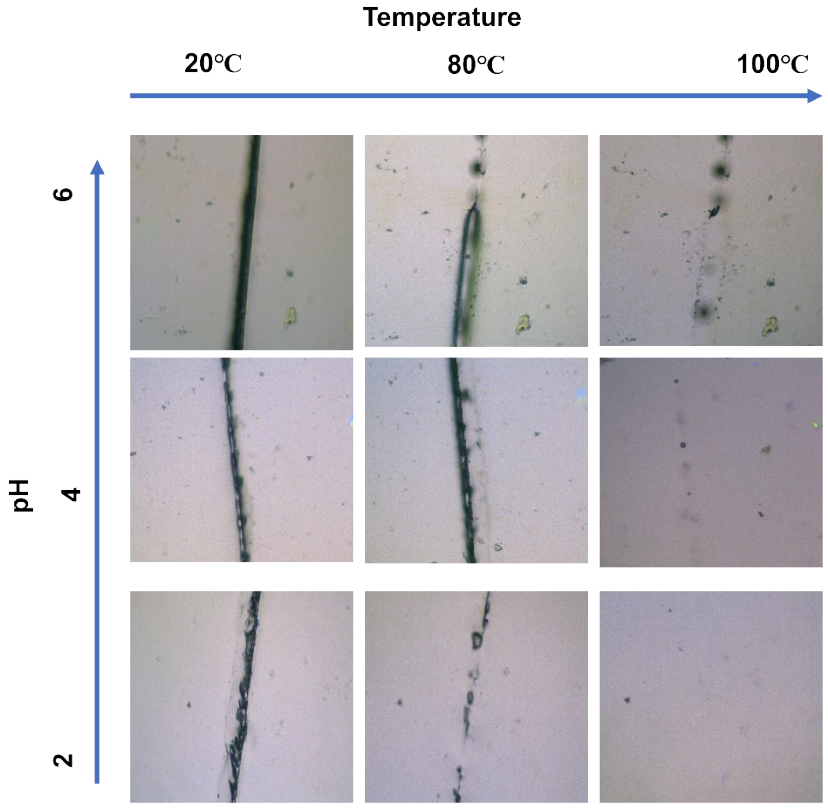


***Fig. S3.*** *Self-Healing efficiency variation with the change in pH from 2-4 at different temperatures ranging from 20-100 °C*

**Section 4-S: Swelling of the crosslinked resin**

The swelling behavior of the acrylic ionomer networks was investigated at different pH values (2 and 4) in both deionized (DI) water and 0.5 M NaCl solution to elucidate the effect of protonation

state and ionic screening on water uptake. Each specimen was oven-dried prior to immersion to ensure normalization of the swelling ratio to the same initial dry mass. The samples were then immersed in media of fixed pH (2 and 4) for identical durations (24 h) under controlled temperature, and the pH of the medium was monitored throughout the test to avoid drift during equilibration. The swelling ratio (Q) was calculated according to the relation:

$$Q_s = \frac{W_s - W_i}{W_i} \quad \text{(eqn. S3)}$$

where Wi is the initial dry weight of the specimen and Ws is the weight after equilibrium swelling. The results are summarized in **Table 1S**.

At pH 2, the films exhibited the highest degree of swelling in DI water, with a calculated Q of 1.89, corresponding to nearly a 190% mass increase relative to the dry weight. This significant uptake is attributed to the almost complete protonation of tertiary amine groups (DMAEMA units), which results in a high density of fixed cationic sites ($R_3NH^+$). The presence of these fixed charges within the polymer matrix generates a substantial Donnan osmotic pressure due to the imbalance of counterion concentrations inside and outside the gel. Consequently, water molecules are drawn into the polymer network to equilibrate the ionic gradient, leading to pronounced swelling. In stark contrast, the same sample at pH 2 immersed in a 0.5 M NaCl solution showed only marginal swelling (Q = 0.11). The abundant external sodium and chloride ions effectively screen the internal cationic charges, neutralizing the osmotic imbalance and thereby suppressing water uptake. This drastic reduction in swelling upon salt addition provides compelling evidence of ionomer formation and the dominance of electrostatic interactions in governing the swelling process. At pH 4, the swelling ratio in DI water was markedly lower compared to pH 2, with values of 0.72 and 0.35 observed across different replicates. Although the amine groups remain largely protonated at this pH, the osmotic pressure is reduced due to a slightly lower degree of ionization and stronger electrostatic association between the protonated amines and lactate counterions. In addition, the glutaraldehyde-derived acetal crosslinks within the network impose steric constraints that limit chain mobility and reduce water penetration. These effects collectively moderate the swelling behavior. When exposed to 0.5 M NaCl, the swelling ratios further decreased to 0.15, consistent with the screening of electrostatic interactions by external salt ions. The collapse in swelling from DI water to saline conditions at both pH values further corroborates the role of ionic interactions

in dictating water uptake. The comparative analysis across pH conditions establishes a clear hierarchy: $\mathbf{Q_{(pH\ 2,\ DI)} > Q_{(pH\ 4,\ DI)} >> Q_{(pH\ 2,\ NaCl)} \approx Q_{(pH\ 4,\ NaCl)}}$. This trend demonstrates that the swelling of the acrylic ionomer is primarily driven by the extent of protonation of pendant amine groups and is strongly modulated by the ionic strength of the medium. At pH 2, the films exhibited the highest degree of swelling in DI water. This pronounced swelling is attributed primarily to the protonation of lactic acid, which significantly reduces the availability of carboxylate anions ($COO^-$) and thereby suppresses ammonium-carboxylate ionic pairing within the network. As a result, ionic crosslinks are effectively diminished under strongly acidic conditions. The loss of these physical crosslinks leads to enhanced chain mobility and reduced network constraints. In addition, the presence of protonated amine groups ($R_3NH^+$) without corresponding counterion pairing results in reduced internal charge screening, generating an osmotic imbalance that drives water uptake. Consequently, the network undergoes substantial expansion, leading to the observed high swelling ratio. These findings not only confirm the successful formation of an ionomeric structure within the lactic acid-modified acrylic polymer but also provide a molecular-level explanation for the observed differences in self-healing and hardness. The enhanced swelling at pH 2 correlates with increased chain mobility and dynamic acetal bond exchange, which promote efficient self-healing. Conversely, the restricted swelling at pH 4 and under saline conditions reflects a denser and more rigid network, which contributes to improved mechanical hardness at the expense of healing efficiency. Such tunable behavior underscores the multifunctionality of these dynamic ionomer networks and highlights their potential for applications requiring a balance between adaptability (healing) and stability (hardness).

**Table 1S:** Weight change in different media

| pH sample | Weight in DI water (mg) | Weight in NaCl (0.5 M) |
|---|---|---|
| pH-2 sample | Wi- 41.7 | Wi-31.8 |
| | Ws-120.5 | Ws-35.4 |
| pH-4 sample | Wi-63.1 | Wi-72.4 |
| | Ws-108.5 | Ws-83.2 |
| pH-6 sample | Wi-78.2 | Wi-57.1 |
| | Ws-105.3 | Ws-78.1 |

**Section 5-S: Self-healing mechanism analysis**

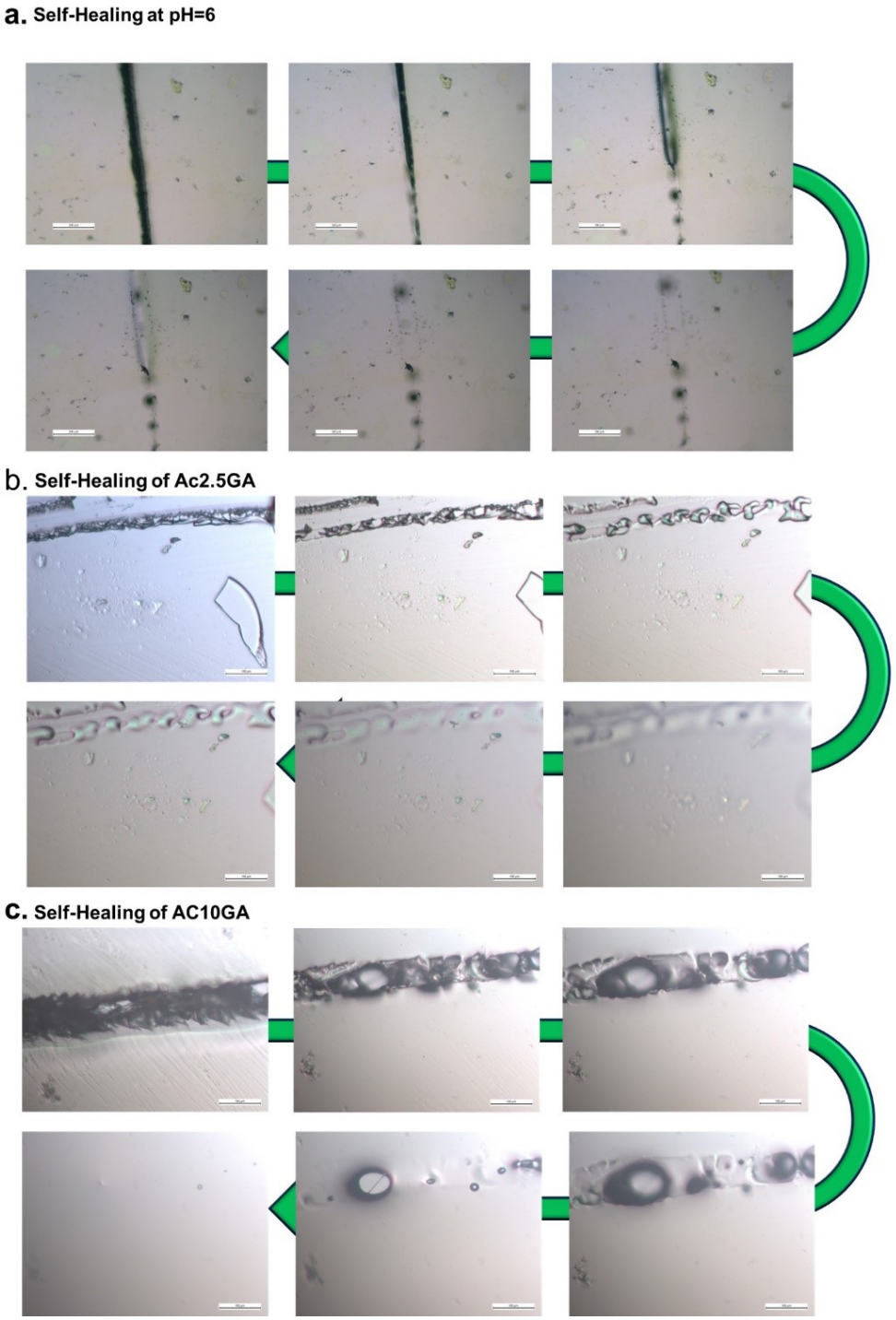


***Fig. S4.*** *Optical microscopy images showing self-healing behavior of coatings at (a) pH 6, i.e. Ac10GAp6, (b) Ac2.5GA, and (c) Ac10GA, demonstrating progressive crack closure under thermal activation at pH 2.*

## Section 6-S: Elemental analysis of coated samples and the silane-modification MWCNT

Elemental mapping confirms the successful incorporation of HDTMS-functionalized MWCNTs within the acrylic coating (**Fig. S5**). The MWCNT-incorporated sample shows a markedly higher Si content (1.9 wt.%) compared to the pristine coating (0.1 wt.%), consistent with siloxane modification and uniform Si distribution across the film. The increased N and O content further reflects the ionomeric and acetal functionalities introduced in the dynamic network.

a.

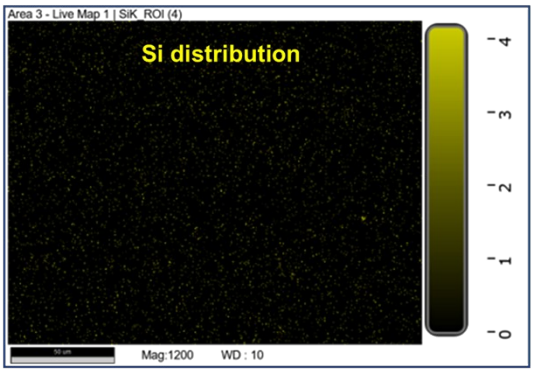


| Element | Weight % |
|---|---|
| C | 54.1 |
| N | 2.9 |
| O | 41.4 |
| Si | 0.1 |

Pristine coating

b.

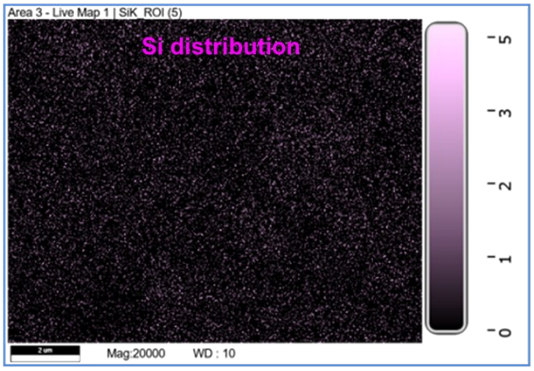


| Element | Weight % |
|---|---|
| C | 76.2 |
| N | 2.7 |
| O | 19.2 |
| Si | 1.9 |

MWCNT-incorporated coating

***Fig. S5.*** *EDX elemental mapping and composition of: a. pristine coating and b. MWCNT-incorporated acrylic coating, highlighting the enhanced Si content and uniform distribution in the nanofiller-modified system.*

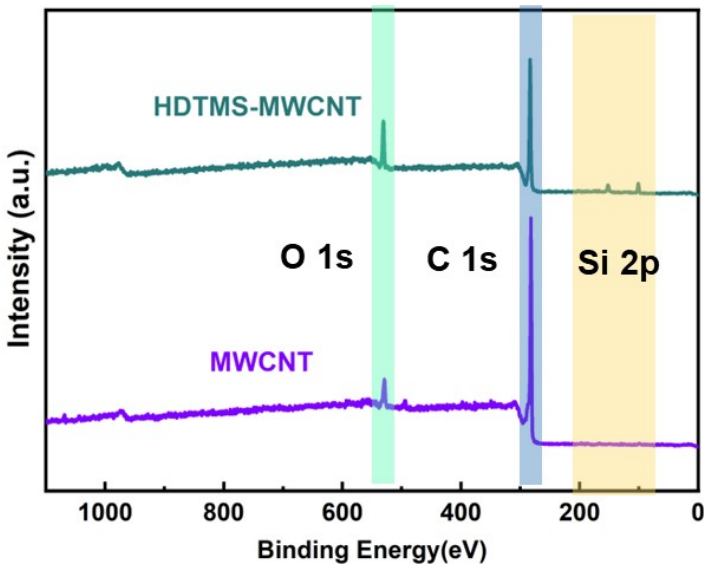


***Fig. S6.*** *Wide-scan XPS spectra of pristine and HDTMS-modified MWCNTs.*

**Table 2S. Summary of elemental composition and binding energies from XPS survey spectra of pristine and HDTMS–MWCNT–incorporated coatings**

| Element | Atomic % (Pristine coating) | Atomic % (HDTMS-MWCNT coating) |
|---|---|---|
| C 1s | 67.3 | 62.8 |
| O 1s | 20.1 | 18.3 |
| N 1s | 2.7 | 2.6 |
| Si 2p | — | 2.8 |
| Total | 100 | 100 |

**Section 7-S: Coating properties**

The physical and mechanical properties of the coatings were evaluated to assess their durability and surface performance (**Table 2S**). Cross-cut adhesion values increased with crosslinker and nanofiller incorporation, improving from 3 (Ac2.5GA) to 5 for Ac10GA and Ac10GA0.05, with further stability at 5 in Ac10GA0.1, indicating excellent substrate bonding across all optimized formulations. Pencil hardness also followed a reinforcing trend, increasing from 4H for Ac2.5GA to 6H for Ac10GA0.1, demonstrating progressive enhancement in scratch resistance due to denser crosslinking and CNT reinforcement. Film thickness varied between 20-28 µm, reflecting

consistent deposition efficiency during the CED process, with slightly higher values observed in CNT-containing formulations, consistent with improved field-assisted deposition. Surface wettability was significantly influenced by filler incorporation: water contact angles increased from 73.5° (Ac2.5GA) to 89.6° for Ac10GA0.05, confirming enhanced hydrophobicity due to HDTMS-modified CNT domains, before slightly decreasing to 85.4° at 0.1 wt.% CNT loading, likely due to agglomeration and loss of uniform roughness. Collectively, these results establish Ac10GA0.05 as the optimal formulation, combining excellent adhesion, mechanical hardness, uniform thickness, and the highest water repellence.

**Table 3S. Physical and mechanical properties of the coatings**

| Sample Name | Cross-cut Adhesion | Pencil Hardness | Contact Angle (°) | Thickness (µm) |
|---|---|---|---|---|
| Ac2.5GA | 3 | 4H | 73.5 | 20 |
| Ac5GA | 3 | 4H | 75 | 22 |
| Ac10GA | 4 | 4H | 79.1 | 22 |
| Ac10GA0.05 | 5 | 6H | 89.6 | 26 |
| Ac10GA0.1 | 5 | 6H | 85.4 | 28 |

**Section 8-S: Self-Healing Efficiency**

The self-healing efficiency is calculated by measuring the cut width at initial (t=0min) and then at t=10min and finally at t=20mins for Ac10GAp2 at 80°C, using equation (S4).

$$H_e = \left(1 - \frac{C_{w0}}{C_{wt}}\right) \times 100\% \quad \text{(eqn. S4)}$$

Where $H_e$ is healing efficiency (%), $C_{wo}$ is the initial crack width (µm), and $C_{wt}$ is the crack width (µm) at the time of analysis.

From the **Fig. S5** it can be confirmed that the healing of the coating at 10 mins is around 99.5% and it shows complete 100% healing at 20 mins.

Electrochemical impedance spectroscopy (EIS) was employed independently to assess the recovery of corrosion protection after healing, but it was not used to calculate the healing efficiency. The fitted EIS parameters before and after healing (12h) are presented in **Fig. S5d**.

After healing, the pore resistance ($R_{po}$) decreases to approximately 10% of the intact coating value, indicating the presence of residual micro-defects and interconnected ionic pathways within the bulk coating matrix that facilitate electrolyte penetration. This suggests that, although the macroscopic crack is visually closed, the nanoscale barrier continuity of the polymer network is not fully restored.

In contrast, the charge-transfer resistance ($R_{ct}$) retains approximately 85% of its original value, demonstrating that the metal/coating interface remains largely protected from electrochemical reactions. This indicates that the self-healing process is particularly effective in re-establishing interfacial isolation, likely through dynamic acetal/hemiacetal bond exchange and ionomeric clustering near the damaged region, which suppress direct electrolyte access to the substrate.

The disparity between $\mathbf{R_{po}}$ and $\mathbf{R_{ct}}$ recovery reflects the inherent nature of dynamic polymeric self-healing systems: rapid macroscopic crack closure occurs through reversible bond rearrangement and chain diffusion, while the complete reconstruction of a dense, defect-free bulk barrier requires more extensive network reorganization. Consequently, physical healing and interfacial corrosion protection can be largely restored, even though the pristine barrier properties of the coating matrix are only partially recovered. Similar behavior has been widely reported for intrinsic self-healing polymer coatings, where visual damage repair does not necessarily correspond to full electrochemical barrier restoration.

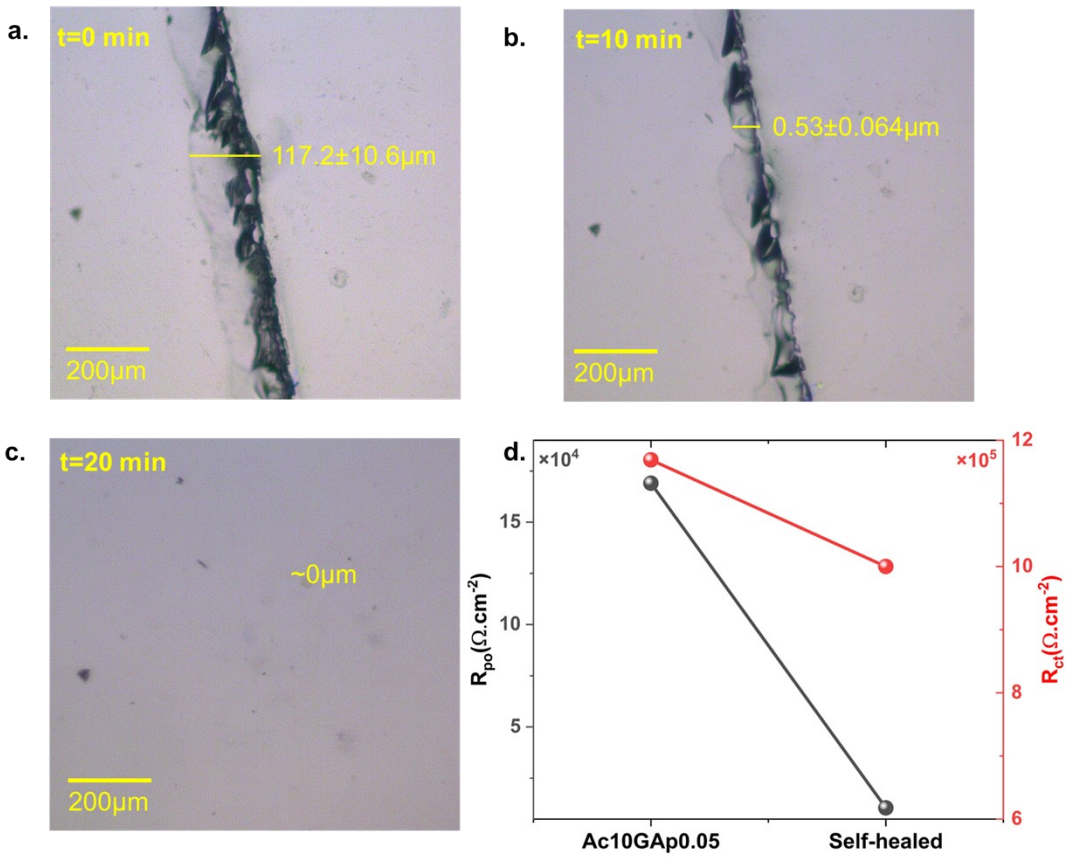


***Fig. S7.*** *Calculation of the self-healing efficiency of the Ac10GA0.05 coating at pH 2 from crack reduction via Image J at a. t=0min; b. t=10min; c. t=20min; d. Change in the* $R_{po}$ *and the* $R_{ct}$ *values of the pristine and after self-healing of the Ac10GA0.05 coating. (maybe a little bigger)*

## Section 9-S: Stability of the Coating System

### Mechanical wear (sand abrasion test):

The hydrophobic stability was assessed using a standardised sand-abrasion test. Although a gradual reduction in water contact angle was observed with increasing abrasion cycles, the coating retained a hydrophobic character even after prolonged abrasion, confirming the robustness of the HDTMS-modified CNT-derived surface architecture. Importantly, after abrasion-induced surface damage, the coating still exhibited effective self-healing upon thermal/acidic stimulation, indicating that the underlying dynamic ionomer–acetal network remains intact and functional despite mechanical wear.

Electrochemical impedance spectroscopy (EIS) was further used to assess the corrosion protection performance after abrasion. As shown in **Fig. S6 a-c**, the Nyquist, Bode magnitude, and phase angle plots recorded after 10-50 abrasion cycles exhibit a gradual decrease in impedance with increasing wear severity. Nevertheless, even after 50 abrasion cycles, the coating maintains a capacitive response and a well-defined phase angle maximum, confirming the persistence of a protective barrier layer. This indicates that although the outer CNT-rich hydrophobic layer is partially removed, the underlying coating matrix remains electrochemically functional.

### UV-aging stability:

UV resistance was evaluated by prolonged UV exposure for 2 weeks, followed by contact-angle measurements. The coating maintained stable hydrophobicity with only a marginal decrease in contact angle, demonstrating that the fluorine-free, siloxane-modified CNT architecture effectively resists UV-induced surface degradation. Furthermore, post-UV-exposure healing experiments confirmed that the self-healing capability is preserved, indicating that dynamic acetal/hemiacetal exchange and ionomeric interactions are not adversely affected by UV ageing.

### Long-term Stability Test:

Overall, these results demonstrate that the coating exhibits good durability against mechanical abrasion and UV exposure, with sustained hydrophobicity and preserved self-healing functionality. The corrosion protection performance after prolonged saline exposure was examined by EIS after 3-28 days of immersion in 3.5 wt.% NaCl solution. As shown in **Fig. S6 f-h**, the

Nyquist and Bode plots exhibit only a moderate decrease in impedance and phase angle values with increasing immersion time, while the coating retains a predominantly capacitive response characteristic of an effective barrier layer. This confirms that the coating maintains its anti-corrosion functionality even after extended exposure to a corrosive marine-like environment.

Overall, these results demonstrate that the coating exhibits good durability against mechanical abrasion, UV ageing, and long-term saline immersion, with sustained hydrophobicity, preserved corrosion resistance, and maintained self-healing functionality. The dynamic ionomer–acetal network remains structurally and chemically stable under harsh environmental conditions, supporting the practical applicability of the coating system.

**Table 4S.** Weight loss and contact angle change with increasing abrasion cycle

| No. of Cycles | Mass Loss (mg) | % Loss (10-4) | Contact Angle (°) |
|---|---|---|---|
| 0 | - | - | 90 |
| 10 | 0.6 | 0.97 | 88 |
| 20 | 0.89 | 1.78 | 84 |
| 30 | 1.12 | 2.41 | 81 |
| 40 | 1.45 | 2.94 | 79 |
| 50 | 2.78 | 5.20 | 72 |

**Section 10-S: Ice Adhesion and Ice Delay Time Calculation**

The ice adhesion could not be calculated due to unavailability of an ice-adhesion tester. However, we did calculate the theoretical ice adhesion parameter from the contact angle of the water droplets to the surface as per the calculation shown by Rønneberg et. al[3]. They considered a drop on a surface with contact angle θ and the surface tension of the water droplet as $\gamma_w$, the surface tension of the substrate as $\gamma_s$ and that of the interface of the substrate and the water droplet as $\gamma_{w,s}$.

From the given scenario we assume the Young's contact angle given by:

$$\gamma_{w,s} + \gamma_w \cos\theta = \gamma_s \text{ (eqn. S5)}$$

The work which is done to remove the ice from the surface is defined as the $W_a$, thermodynamic work of adhesion. This work of adhesion is given by:

$$W_a = \gamma_s + \gamma_i - \gamma_{i,s}$$ (eqn. S6)

where subscript i denotes ice, and represents the work required to break the bond between the ice and the surface and form two new surfaces. On combining equation S5 and S6 we derive:

$$W_a = \gamma_i + \gamma_w \cos\theta + (\gamma_{w,s} - \gamma_{i,s})$$ (eqn. S7)

When considering the commonly accepted assumption that the surface energies of water and ice are similar, and thus also the interfacial energies are similar, Equation (S7) can be reduced to:

$$W_a = \gamma_w (1 + \cos\theta)$$ (eqn. S8)

The ice adhesion strength τ is commonly defined as the maximum force required to detach the ice from the surface divided by the contact area of the ice solid surface, given by:

$$\tau = \frac{F_{max}}{A}$$ (eqn. S9)

The ice adhesion strength is thus a measure of pressure, and when considering that the work of adhesion is a measure of energy, it can be assumed in general that the relation between the ice adhesion strength and the work of adhesion is given by:

$$W_a = \tau A \delta$$ (eqn. S10)

where A is the surface area of the ice and δ is a characteristic measure of the removal distance between the ice and surface. Combining Equations (S8) and (S10) we derive:

$$\tau = \frac{\gamma_w}{A\delta}(1 + \cos\theta)$$ (eqn. S11)

Since the surface tension of water, the surface area of the ice and the removal distance are constant, the ice adhesion parameter is directly proportional to the contact angle via the factor (1+cos θ). By using this logic, we calculated the theoretical ice adhesion parameter for the bare and the coated substrate. It was seen that the application of the coating decreased the adhesion parameter by a factor of 1.9. So, we can theoretically conclude that the application of the MWCNT-acrylic coating halved the adhesion of the ice as compared to the bare substrate.

The contact angle increases from 79° to 90°. The addition of the MWCNTs results in the formation of nanoscale roughness which hinders the formation of the ice by reducing interfacial contact area. We calculated the freeze delay time for Ac10GA coated glass panel which shows a freeze delay time of around 2000s, which is longer than the bare glass panel but lower as compared the Ac10GA0.05.

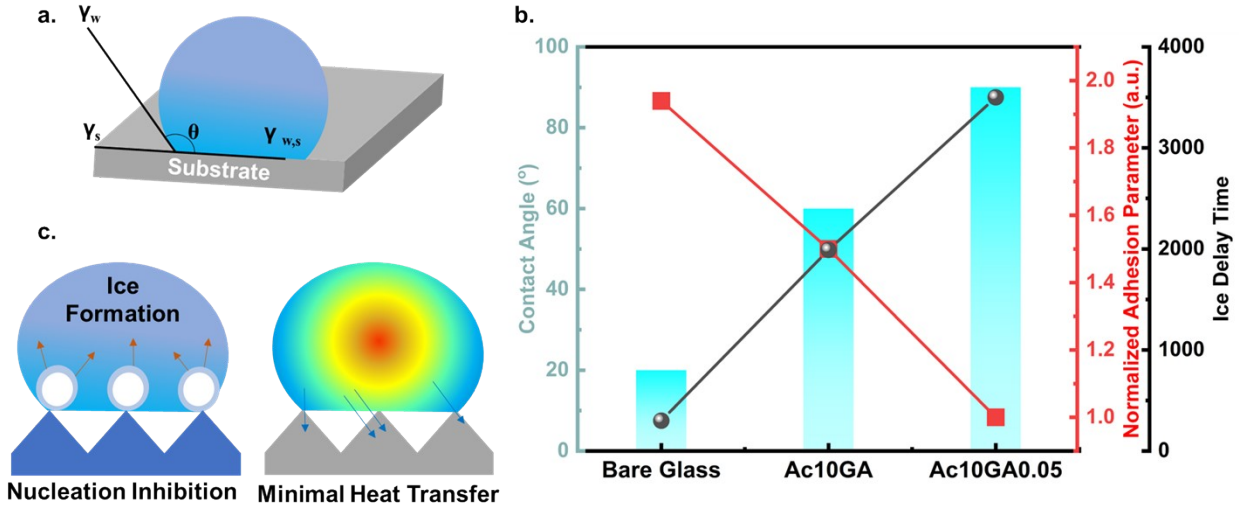


***Fig. S8.*** *a. The basis for the calculation of the ice adhesion parameter from the contact angle calculation; b. comparison of the contact angle, adhesion parameter and the ice delay time for the bare, Ac10GA and the Ac10GA0.05 coated glass samples; c. the rationale behind the increased ice delay time due to the nano-roughness due to the introduction of the MWCNTs.*

**Section 11-S: Coating bath Stability**

The stability of the cathodic electrophoresis (CED) baths was evaluated after preparation to assess their suitability for practical and scalable application. For the optimized formulation containing 0.05 wt.% HDTMS-modified MWCNTs, the bath remained visually stable for more than two months under static storage conditions, with no significant sedimentation observed. Only a minimal amount of CNT deposition was detected at the bottom of the container, which could be readily re-dispersed by gentle mechanical stirring at 300 rpm for 10 min, restoring a homogeneous and fully functional deposition bath.

In contrast, formulations containing a higher CNT loading (0.1 wt.%) exhibited noticeable settling over time, attributed to increased filler-filler interactions and partial agglomeration. This behavior

further confirms 0.05 wt.% as the optimal CNT concentration, providing a balance between dispersion stability, functional performance, and process reliability.

These observations highlight the long-term bath stability and practical scalability of the optimized CED formulation for multifunctional coating applications.

**Section 12-S: Comparison of the Coating Properties**

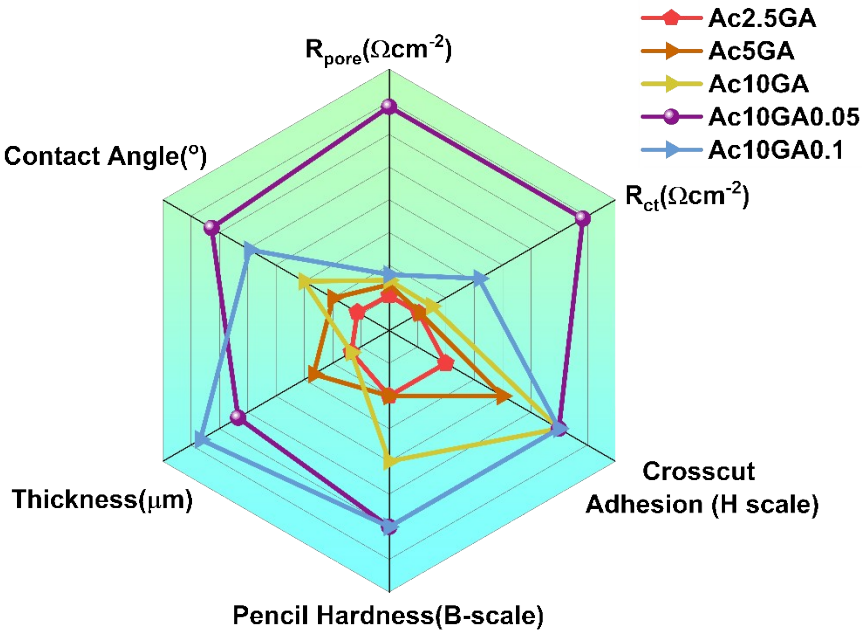


***Fig. S9****. Radar plot summarizing the comparative performance of the coating systems, highlighting the balanced enhancement in key properties, including corrosion resistance, hydrophobicity, self-healing efficiency, anti-icing behavior, and recoatability, for the optimized formulation relative to control samples.*

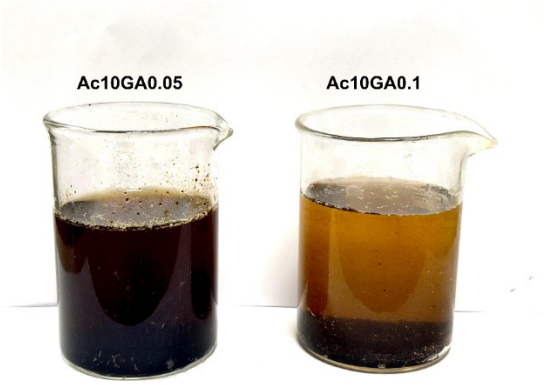

***Fig. S10.*** *Stability of electrodeposition baths containing HDTMS-modified MWCNTs: a. The optimized concentration of 0.05wt.% MWCNTs ensures uniform CNT distribution and stable bath behavior conducive to coherent coating deposition; while 1 wt.% MWCNTs showing phase separation and sedimentation (after 1 month).*

## References:


(1) Sen, S.; Chatterjee, A.; Ramakanth, D.; Singh, S.; Maji, P. K. Recent Advances in Cathodic Electrodeposition Coatings with Special Reference to Resin Materials: A Comprehensive Review. *Prog. Org. Coat.* **2024**, *190*, 108387. https://doi.org/10.1016/J.PORGCOAT.2024.108387.

(2) Chatterjee, A.; Yadav, A.; Sen, S.; Ghosh, S.; Choudhary, N.; Dey, N.; Mishra, S.; Maji, P. K. Polymer-Modified Nonwovens: Functional Surfaces for Separation, Sensing, Biomedical and Smart Textile Applications. *J. Mater. Chem. A Mater.* **2026**, *14* (6), 3210–3252. https://doi.org/10.1039/d5ta08703a.

(3) Rønneberg, S.; Xiao, S.; He, J.; Zhang, Z.; Rønneberg, S.; Xiao, S.; He, J.; Zhang, Z. Nanoscale Correlations of Ice Adhesion Strength and Water Contact Angle. *Coatings 2020, Vol. 10,* **2020**, *10* (4). https://doi.org/10.3390/COATINGS10040379.